Multiscale Reconstructions, Effective Elastic Properties, and Ultrasonic Responses of Kerogen Matter Based on Digital Organic Shales

YING RAO[1,2,3], LI-YUN FU[4,5], ZHI-WEI WANG[4,5], AND BO-YE FU[1,3]

[1]Key Laboratory of Petroleum Resources Research, Institute of Geology and Geophysics, Chinese Academy of Sciences, Beijing 100029, China
[2]College of Earth and Planetary Sciences, University of Chinese Academy of Sciences, Beijing 100049, China
[3]Innovation Academy for Earth Science, Chinese Academy of Sciences, Beijing 100029, China
[4]Key Laboratory of Deep Oil and Gas, China University of Petroleum (East China), Qingdao 266580, China
[5]Laboratory for Marine Mineral Resources, Qingdao National Laboratory for Marine Science and Technology, Qingdao 266071, China

Corresponding author: Li-Yun Fu (lfu@upc.edu.cn)

ABSTRACT Organic shales usually present significant heterogeneities in rock textures and reservoir properties due to differing kerogen contents and morphologies, subsequently impacting shale elastic properties and acoustic responses. Numerical upscaling of digital organic shales to evaluate effective elastic properties and acoustic responses has important implications for source rocks and unconventional reservoir characterization. We propose a modeling framework that includes the multiscale reconstruction of kerogen distributions, the numerical modeling of effective elastic properties, and the acoustic response to evaluate the contribution of organic matter. Based on digitized images of the microstructure of Longmaxi black shale samples obtained by X-ray CT, the kerogen components are identified and decomposed into different-level slices in terms of organic matter sizes and morphologies. Multiscale random media reconstruction is applied to these kerogen slices, with synthetic kerogen distributions validated by original counterparts. A finite-element method is used to model the effective elastic properties of digital organic shales, by which we investigate the effect of different kerogen contents and organic matter morphologies. We use a rotated staggered-grid finite-difference method to simulate ultrasonic wave propagation in digital organic shales to evaluate the response of different kerogen contents and organic matter morphologies. Numerical examples show that the multiscale random media method can be applicable to natural organic shales for the reconstruction of kerogen distributions. The elastic properties mainly depend on kerogen contents, with less influence by organic matter morphologies. The ultrasonic scattering effects become stronger for higher kerogen contents with smaller rounding coefficients. Our results confirm the applicability of the proposed modeling framework to support unconventional reservoir characterization. The purpose of this study is to provide the possibility of indicating the sweet point of shale.

INDEX TERMS Digital organic shales, effective elastic properties, kerogen contents, multiscale reconstructions, organic matter morphologies, ultrasonic responses.

I. INTRODUCTION

As potential unconventional resources, organic shales have been extensively studied in the last decade. The characterization of shale properties, particularly kerogen abundance and type, is an important part of resource assessment [1]. However, due to the limited investigations of organic-rich

The associate editor coordinating the review of this manuscript and approving it for publication was Gokhan Apaydin.

samples, the dynamic and elastic behavior of organic matter is a long-standing problem in geophysics [2]. Rock physics models facilitate the interpretation of sonic measurements and seismic responses for organic shales. Digital organic shale images are used to digitize the pores and minerals of organic shale and then carry out numerical simulations to obtain the properties of the rock, such as the elastic modulus. The workflow mainly includes the following steps [3]: (a) digital imaging of rocks (e.g., high-resolution 3D CT

scanning) to resolve their microstructure; (b) separation of the pores and minerals; and (c) simulation of physical processes in the microstructural image to determine their effective properties. With digital organic shales, the aim of this study is to reconstruct the distribution of kerogen grains and model their effective elastic properties, followed by simulating ultrasonic responses to evaluate the contribution of different kerogen contents and grain morphologies [2].

Organic matter needs to be well understood in terms of maturity levels, morphologies, and distribution features [4]. The former has been extensively addressed, and three maturity levels [5], [6] significantly affect the effective elastic properties of organic shales [1]. The latter two should not be neglected in the evaluation of either shale-gas rock properties or effective elastic properties. Analyses by Zargari *et al.* [7] and Yenugu [8] imply that the physical and chemical processes of kerogen maturation strongly impact the morphology and distribution of organic matter. Based on petrographic and SEM observations, organic matter is generally irregular in morphology, multi-sized, and randomly distributed in shales. In particular, the distribution of organic matter plays an important role in determining the elastic properties of organic-rich shales, which in turn affects production-induced stress changes [9]. Therefore, it is critical to integrate the morphology and distribution of organic matter into organic rock physics models.

Multiscale reconstruction of source rock heterogeneities provides an effective means to predict the spatial distribution of organic matter based on cores from several wells. The literature abounds with works aimed at the core-scale reconstruction of brittle minerals and pore structures of shales but is rarely dedicated to organic matter. The reconstruction methods commonly used include truncated Gaussian random media, simulated annealing, sequential indicator simulation, multiple-point statistics, and various hybrid methods [10]–[14]. A comprehensive review of core-scale numerical reconstruction methods with detailed applications can be found in Ji *et al.* [15]. The most typical algorithms of object-based techniques result from random media theory described by mathematical tools such as autocorrelation functions and power spectral density functions [16]–[22]. However, these methods are only suitable for a single-scale or single-component reconstruction of digital cores and are less accurate for strongly heterogeneous shales. Based on the random distribution of organic matter in a petrographic slice of digital core, we propose a multiscale random media reconstruction of kerogen distribution by decomposing organic matter into individual single-scale components in terms of their sizes and morphologies, followed by single-scale random media reconstruction and composition.

The effective elastic properties of organic shales have been extensively studied by different methods, for example, analytical models [23] based on effective medium theory, the modified Backus averaging method [5], the Hashin-Shtrikman lower-bound model [24], the hybrid approach of Backus averaging, Krief/Gassmann models [25], [26], the solid substitution model [27], [28], the rock-physics template to correlate kerogen maturation and elastic behaviors of shale [1], and rock-physics modeling of elastic properties for prestressed organic shales [29]. The analytical model for effective elastic properties is only applicable to simple media. It is difficult to solve the effective elastic properties of rock components with arbitrary shapes. Numerical methods are universal techniques to model complex media. Elastic numerical modeling has been widely used for digital cores [3], [30]–[34]. Substantial progress has been made in the numerical modeling of kerogen contents. However, few studies have investigated the effect of the morphology and distribution of organic matter. For general applicability to complex organic shales in this study, a finite-element (FE) method is used to estimate the effective elastic properties from a heterogeneous digital core, with particular attention given to the distinction of elastic responses of different morphologies and distributions of organic matter. The elastic model allows its physical properties to vary laterally and vertically, thereby mapping heterogeneous rock properties in detail.

The ultrasonic response of brittle minerals and pore structures has been extensively addressed in numerical simulations, but with no publications relevant to organic matter, the effect of organic matter content, shape and distribution on the ultrasonic response is lacking. Short-wavelength wave scattering has long been the focus of geophysicists [35]–[37]. The scattering effect of small-scale heterogeneities called coda [35], [38] has been widely used to analyze the inhomogeneous scale in the lithosphere [39], [40]. Ultrasonic wave propagation in heterogeneous porous rocks is an extremely complex process. Laboratory ultrasonic measurements provide data on the interaction between ultrasonic waves and small-scale random heterogeneities. Numerical simulation of the ultrasonic response of digital cores enables insights into the effect of microstructures [41]–[46]. Digital core technologies can capture mineral components and microstructures at a micrometer resolution, making it possible to simulate wave propagation in authentic heterogeneous rocks [28], [34]. Several key issues challenge such numerical simulations, such as digital imaging of heterogeneities, estimation of effective elastic constants, numerical dispersion at high frequencies, and strong heterogeneities. This study applies a rotated staggered-grid (RSG) finite-difference (FD) method [47], [48] of Biot's poroelastic equations to simulate ultrasonic wave propagation in digital organic shales, especially highlighting the ultrasonic scattering of kerogen contents and their morphologies. The RSG-FD method, implemented by eight-order (for spatial derivatives) and two-order (for time derivatives) FD operators, can improve numerical stabilities and accuracies for high frequencies and strong heterogeneities because no averaging of elastic moduli is required in an elementary cell. To enable a controllable absorbing boundary for numerical simulations at the core scale, we use an unsplit convolutional perfectly matched layer (CPML) absorbing boundary [49], [50].

The paper is organized as follows: first, a core-scale reconstruction of kerogen distributions is conducted by a multiscale random media method for a group of digital shale cores with different kerogen contents and morphologies. In particular, single-scale decomposition and multiscale composition of organic matter is illustrated in detail. Then, FE numerical modeling of effective elastic properties is implemented for digital organic shales by focusing on elastic responses to the content and morphology of organic matter. We next apply the RSG-FD numerical simulation of Biot's poroelastic equations to ultrasonic wave propagation in digital organic shales followed by a coda analysis of ultrasonic scattering with kerogen contents and their morphologies.

II. MULTISCALE RECONSTRUCTION OF KEROGEN DISTRIBUTIONS

Organic shales contain inorganic and organic components. The former includes rigid grains of quartz and calcite and ductile grains of clay typically undergoing initial sedimentation, dehydration, compaction, and cementation, whereas the latter involves complex physical and chemical changes along with the sedimentation of fine-grained inorganic particles. Therefore, the size, density, and morphology of organic matter is distributed heterogeneously, even inside the same sedimentary facies. Reconstructing the spatial distribution of organic matter using core samples from different wells plays an important role in determining development schemes. In this section, we take the Longmaxi organic shale as an example to demonstrate the digital petrography, distribution characteristics, and detailed reconstruction of organic matter.

A. DIGITAL CORE OF THE LONGMAXI FORMATION SHALE

Black organic shales from the lower Silurian Longmaxi Formation in Jiaoshiba Town in the eastern Sichuan fold belt have thick reservoirs, dense distributions, and rich organic matter and have supported the main shale-gas exploration and development blocks in China. Figure 1 shows a shale sample taken from an outcrop in this area. Rock physics experiments show that total organic carbon (TOC) in black shale has an average content of 2.18%. The main brittle minerals are quartz (average content of more than 45%) and feldspar [51], [52].

With an 800 μm diameter core, we reconstructed a digital core with 0.65 μm pixels based on X-ray fluorescence computed tomography. Figure 2a shows the resulting high-resolution 3D image chosen at the center of the core sample (size of 390 μm × 390 μm × 390 μm). It consists of 3.2 million slices with a total of 600 × 600 × 600 pixels. Pixel colors indicate the X-ray absorbability of varying components, with red to green indicating small to large absorption coefficients. Figure 2b is a 2D slice in the xy-direction. Various minerals, pores/fractures, and kerogens are clearly identified in local amplification (see Figure 2c) due to absorption differences. The higher the absorptivity is, the greater the grayscale value is; white represents pyrites with the highest absorptivity, black indicates pores/fractures with the lowest

FIGURE 1. Longmaxi Formation shale sample from an outcrop in Jiaoshiba town, Chongqing city.
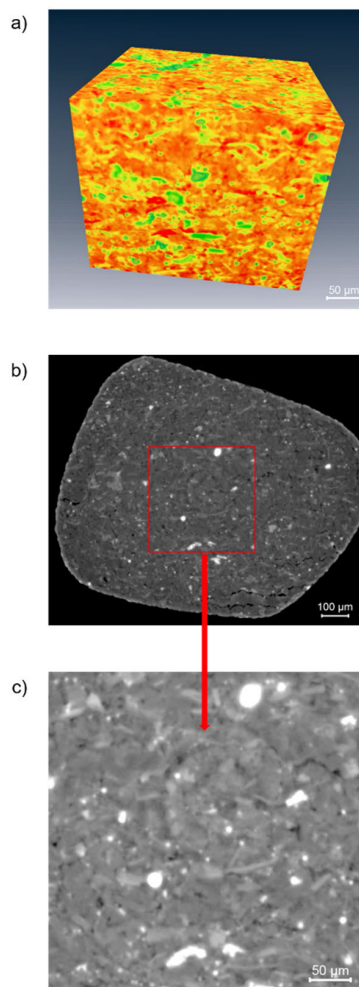

FIGURE 2. Reconstructed 3D image of the Longmaxi shale core (a) and its 2D slice in the *xy*-direction (b) with an enlarged display (c) of the square.

absorptivity, and gray denotes kerogens and other minerals. Table 1 shows the absorptivity of minerals in the core sample.

B. MULTI-COMPONENT AND MULTISCALE DECOMPOSITION

Various components, such as brittle minerals, pores, and kerogens, vary widely in their morphological characteristics as well as in their sizes, which presents an irregular

TABLE 1. Absorptive capacities of X-rays of minerals at 20 keV.

Mineral	Qtz	Or	Dol	Cal	Py
X-ray absorption (cm^{-1})	6.5	10.3	10.5	15	76.7

distribution. Such strong heterogeneities are difficult to model using single-scale and single-component methods. As shown in Figure 2, the kerogen distribution is extracted by a multi-threshold segmentation and then decomposed into different-scale components of size. A multiscale random method is proposed to mathematically reconstruct the kerogen distribution of different scales. This reconstruction scheme provides a potential application; that is, kerogen distributions can be modeled for individual wells and interpolated under the constraint of sedimentary microfacies to build a regional distribution for target formations.

Based on the absorptivity of different components, we can implement the multi-threshold segmentation of digital core images. The basic idea of segmentation [2], [53] is to divide a grayscale histogram into different categories through multiple thresholds. The optimal segmentation threshold can be obtained by maximizing the interclass or minimizing the intraclass variance of categories. Figure 3 displays 2D slices of the Longmaxi-shale digital image segmented by the multi-threshold method. The major components can be classified into four types: Type 1 (pores with a content of 5.69%), Type 2 (brittle minerals with a content of 25.53%), Type 3 (background media with a content of 61.49%), and Type 4 (kerogens with a content of 7.29%), with each type exhibiting obvious heterogeneity in size and morphology. We decompose the kerogen type into three single-scale slices according to its geometric scale, as shown in Figure 4, accounting for 3.58%, 2.22%, and 1.49%, respectively. The red spots denote kerogens, light blue denotes mineral type 2, gray denotes mineral type 3, and dark blue denotes pyrite. In particular, the large-scale kerogen distribution is nonuniform in morphology and presents a hollow structure due to the existence of pores.

C. MULTISCALE RANDOM MEDIA RECONSTRUCTION

The multiscale random media reconstruction of kerogens consists of reconstructing individual single-scale components and then synthesizing them in terms of their proportions by the following equation:

$$KEROGEN = \sum \alpha_i A_i, \quad i = 1, 2, 3, \tag{1}$$

where A_i and α_i are the reconstructed counterpart and its proportion ratio of the ith scale component, respectively. The media reconstruction of each scale component requires three parameters: the autocorrelation lengths a and b in the horizontal and vertical directions and the rounding coefficient n. These parameters need to be estimated carefully to ensure that the average size and roughness of reconstructed kerogens can approximate those of original kerogens. In this paper, we use an intermixed autocorrelation function of $n = 0.6$, 0.7, and
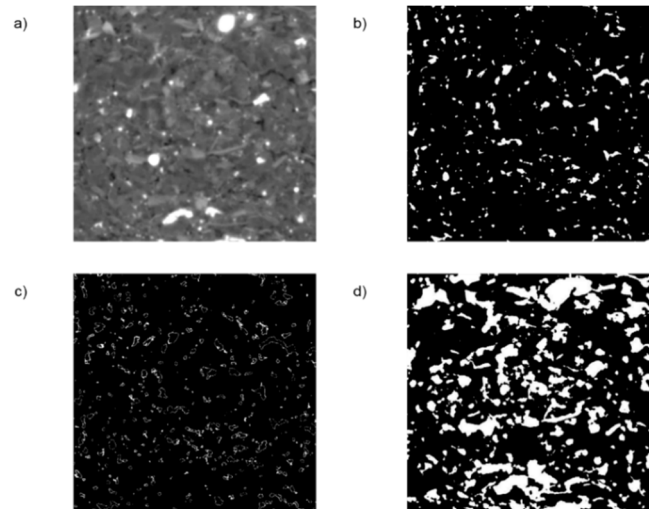

FIGURE 3. 2D slices of the major components in Longmaxi shale in the *xy*-direction: digital core (a), pores (b), kerogens (c), and brittle minerals (d).

0.8 to model large-, middle-, and small-scale kerogen components, respectively.

Figure 5 shows the reconstructed kerogens for three scales of components, as shown in Figure 4, using different media parameters. The red spots denote kerogens, light blue denotes mineral type 2, gray denotes mineral type 3, and dark blue denotes pyrite. The reconstructed middle- and small-scale kerogen distributions agree well with the corresponding original distributions shown in Figures 4b and 4c. Small discrepancies in contrast to Figure 4a, however, are observed in the reconstructed large-scale kerogen distribution. This is because large-scale kerogens are usually distributed along pores and therefore present specific morphologies. The media reconstruction of kerogen distributions can be validated by subsequent correlation analyses.

D. CORRELATION ANALYSES

The following power-spectrum function is often used to describe random reconstruction media:

$$S(f) = e^{-k|f|}, \tag{2}$$

where f is the frequency and $k(0 < k < 1)$ indicates the size of medium particles. Large values of k describe large particles, with the corresponding power-spectrum curves decaying rapidly. The power-spectrum density of a signal can be obtained by its autocorrelation function as follows:

$$
\begin{aligned}
R(\tau) &= \int_{-\infty}^{+\infty} exp(-k|f|) \, exp(i2\pi f\tau) \, df \\
&= \frac{2k}{k^2 + 4\pi^2\tau^2},
\end{aligned} \tag{3}
$$

where τ is the position difference in the spatial domain. Autocorrelation is defined as the Pearson correlation [54] of two random processes in statistics. Compared to the term $4\pi^2\tau^2$ ($\tau \neq 0$), the term k^2 is very small since $0 < k < 1$
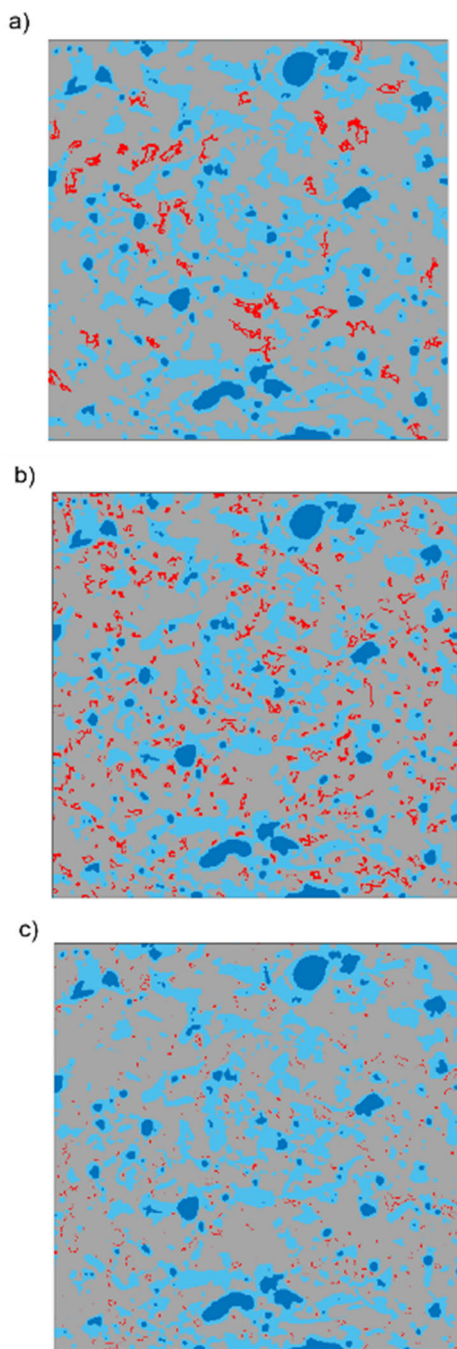
FIGURE 4. Multiscale decomposition of kerogens: large scale (a), middle scale (b), and small scale (c). The red spots denote kerogens, light blue denotes mineral type 2, gray denotes mineral type 3, and dark blue denotes pyrite.

FIGURE 5. Reconstructed kerogen distributions for three scales of components: large scale (a), middle scale (b), and small scale (c) using an intermixed autocorrelation function with different media parameters. The red spots denote kerogens, light blue denotes mineral type 2, gray denotes mineral type 3, and dark blue denotes pyrite.

and can be neglected. We have the following equation:

$$R(\tau) = \frac{k}{2\pi^2\tau^2}. \tag{4}$$

k increases with increasing particle size, with the corresponding $R(\tau)$ varying relatively slowly.

With the autocorrelation function curve $R(\tau)$, we can determine a characteristic parameter that is defined as the effective width of the primary peak at the $R(\tau)$ value when it
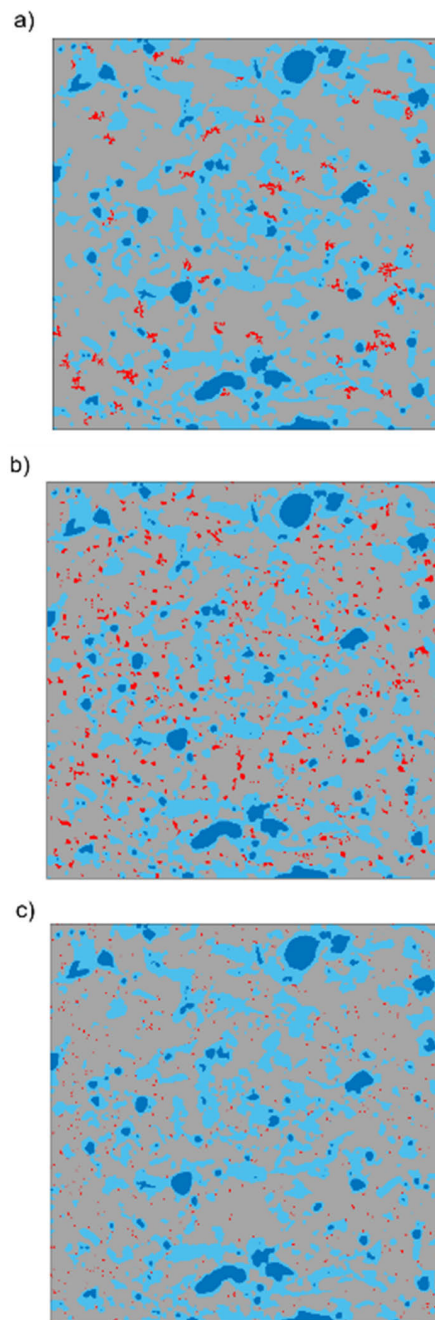
is reduced to 1/e. Figure 6 compares the $R(\tau)$ curves at three scales of original and reconstructed kerogens. In general, the correlation of two signals is defined as strong correlation by their correlation coefficient greater than 0.8, weak correlation by the correlation coefficient between 0.3 and 0.8, and irrelevant by the correlation coefficient below 0.3. From Figure 6, we see that both the original and reconstructed kerogens present strong correlations for all scales, with effective width errors (EWEs) of 0.004, 0.002, and 0.005, respectively.
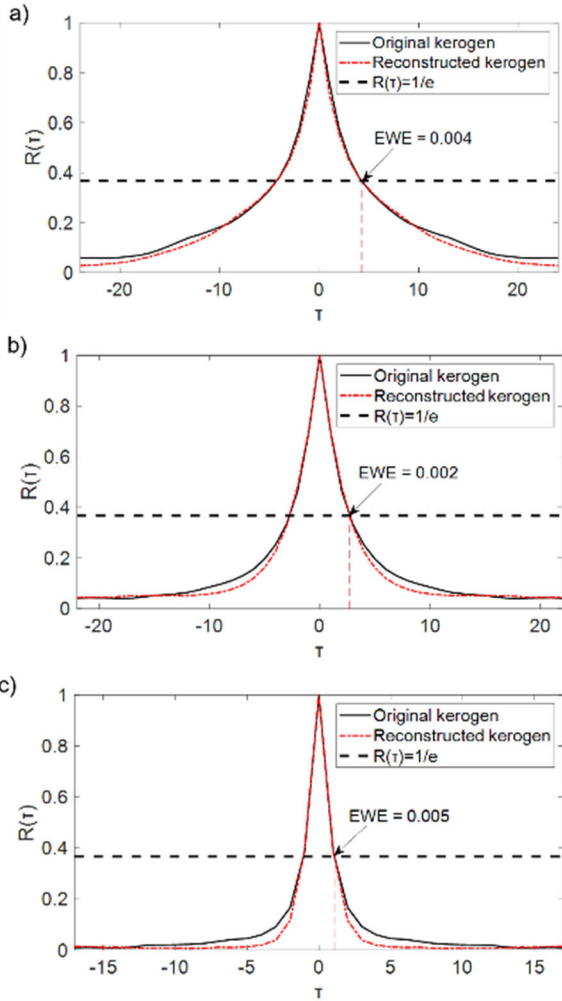
FIGURE 6. Autocorrelation function curves of original and reconstructed kerogens at large (a), middle (b), and small (c) scales.

FIGURE 7. Comparison of original (a) and reconstructed (b) kerogen slices.

The reconstructed kerogens at three scales are synthesized in terms of their proportions using equation (1). The resulting kerogen digital core is shown in Figure 7 with comparison to the original. Similarly, the red spots denote kerogens, light blue denotes mineral type 2, gray denotes mineral type 3, and dark blue denotes pyrite. Both seem to have some discrepancies because of the error in the rounding coefficient used to model the morphology of kerogen particles. To measure their discrepancy, we calculate the autocorrelation function curve of the original and synthesized kerogen distributions, as shown in Figure 8. We see that the kerogen slice reconstructed by the multiscale method with EWE = 0.07 is much better than that reconstructed by the conventional single-scale method with EWE = 0.76. Therefore, the multiscale media method is an effective tool to reconstruct the distribution and morphology of heterogeneous kerogens.

III. ELASTIC MODULI MODELING OF ORGANIC MATTER
The effective elastic property of organic shales is essential to interpret sonic measurements and seismic responses
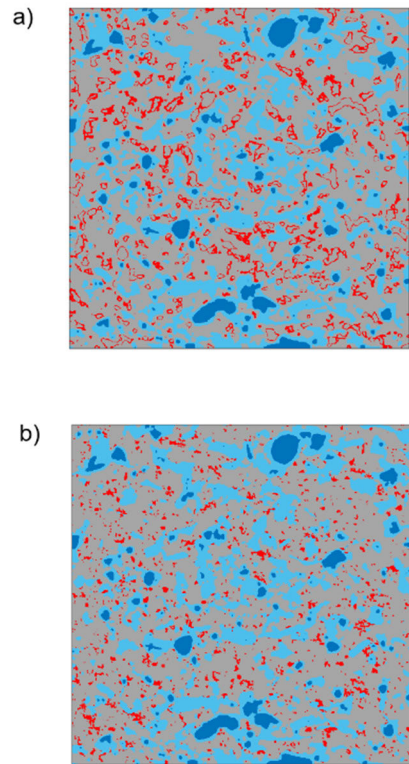
for identifying sweet spots and characterizing source rocks. Kerogen contents and shapes affect the effective elasticity of organic shales. In this section, we first validate the FE numerical method by analytical models for elastic modulus modeling. Then, a comprehensive numerical investigation of effective elastic properties is conducted for shale samples with different contents and morphologies of organic matter.

A. ELASTIC PROPERTIES OF DIFFERENT MINERAL PHASES IN THE LONGMAXI SHALE
Based on the absorption of different mineral phases listed in Table 1, each pixel in the digital image of the Longmaxi shale can be classified as one mineral phase with specific values of equivalent bulk moduli (K) and shear moduli (G). Among the four types of mineral phases in the Longmaxi-shale digital image shown in Figure 3, Type 2 (brittle minerals) and Type 3 (background media) are dominated by quartz and clay, respectively. Pyrite is taken as Type 5 because of its very special elastic properties.

Based on the percentage of minerals inside a specific mineral phase, we can calculate its equivalent values of K and G by the average modulus estimation [55]. For example, the proportions of quartz, kaolinite, and montmorillonite in Type 2 are $\varphi_1 = 6\%$, $\varphi_2 = 92\%$, and $\varphi_3 = 2\%$,, respectively. The bulk modulus (K_{M_2}) for Type 2 can be calculated as follows:

$$K_{M_2} = K_1 \times \varphi_1 + K_2 \times \varphi_2 + K_3 \times \varphi_3 = 34.15 GPa, \quad (5)$$
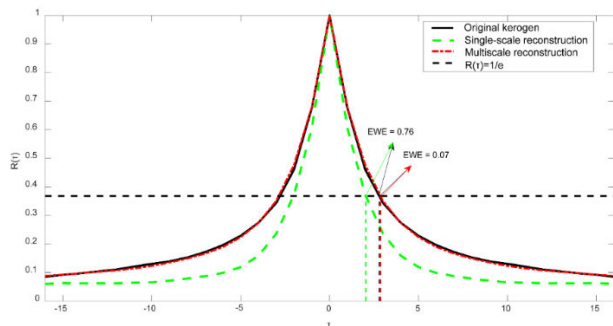
FIGURE 8. Comparison of autocorrelation function curves for original and reconstructed kerogens by multiscale and single-scale random media methods.

where $K_1 = 1.5\,\text{GPa}$, $K_2 = 37\,\text{GPa}$, and $K_3 = 1.2\,\text{GPa}$ represent the bulk moduli of kaolinite, quartz, and montmorillonite, respectively [56]. Likewise, the shear moduli for Type 2 can be computed as $G_{M_2} = 7.6\,\text{GPa}$. For Type 3, the bulk and shear moduli can be obtained in the same way, giving $K_{M_3} = 66.14\,\text{GPa}$ and $G_{M_3} = 34.48\,\text{GPa}$. The equivalent volume moduli K, shear moduli G, and densities of all the types are summarized in Table 2.

TABLE 2. Equivalent bulk moduli K, shear moduli G, and density ρ of all the types ([a] Simmons and Birch [57]; [b] Blangy [58]; [c] Zhao et al. [1]).

Equivalent Elastic Properties	Type 1	Type 2	Type 3	Type 4	Type 5
	Pores (Gas/Oil)	Kaolinite, Quartz, Montmorillonite	Illite, Calcite, Feldspar, Dolomite, Gypsum	Kerogen	Pyrite
Bulk Moduli (GPa)	0.04/0.7	34.15	66.14	5[c]	147.4[a]
Shear Moduli (GPa)	0	7.6	34.48	3.5[c]	132.5[a]
Density (g/cm³)	0.717×10⁻³/0.8	1.66	2.64	1.3[b]	4.93[a]

B. VALIDATION OF FE NUMERICAL MODELING BY ANALYTICAL MODELS

Two solid substitution models are used to compare with FE numerical modeling. One model [59] (called the C&S model in this study) is based on the generalization of Gassmann equations for porous media saturated with a solid material, which assumes that the rock matrix is a homogeneous isotropic medium. The second model [60] (called the S&M model in this study) extends the C&S model to heterogeneous media by using reciprocity. Both models have been applied to study the effect of kerogen contents on the elastic properties of organic shales [28].

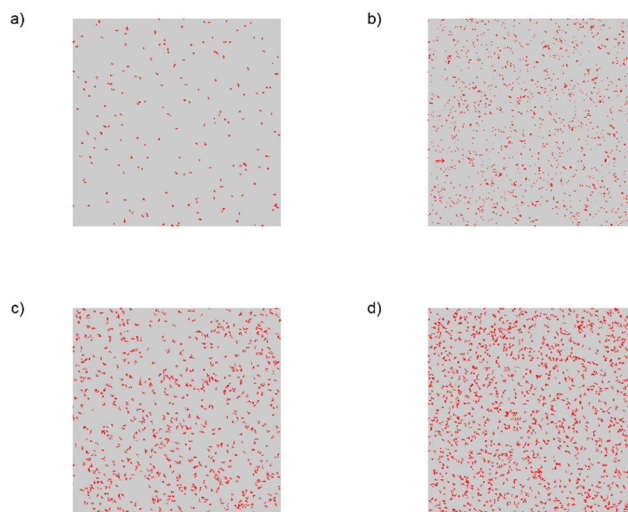Figure 9 shows four kerogen models generated by random media using the rounding coefficient n = 0.6. The kerogen

FIGURE 9. Four kerogen models generated by random media using the rounding coefficient $n = 0.6$. The kerogen content accounts for 1% (a), 3% (b), 5% (c), and 8% (d).
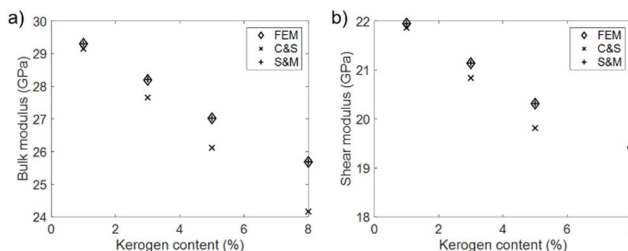

FIGURE 10. Comparison of effective bulk (a) and shear (b) moduli versus kerogen contents by FEM, C&S, and S& M.

contents account for 1%, 3%, 5%, and 8%, respectively. The resultant equivalent elastic properties by FEM, C&S, and S&M are compared in Figure 10. We see that the FE numerical results agree well with those of the S&M model, whereas the modeling accuracies of the C&S model are gradually reduced with increasing heterogeneities in the distribution of kerogen matter. The modeling accuracy of the S&M is controlled by two parameters that represent the effects of kerogen moduli on the saturated medium bulk and shear moduli. For multiscale distributions or complex morphologies of kerogen matter, these two parameters become unstable and reduce the accuracy of S&M [28]. The FE numerical method is universally valid for general applicability to complex organic shales.

C. EFFECT OF KEROGEN CONTENTS ON EFFECTIVE ELASTIC PROPERTIES

Digital core techniques facilitate the investigation of the influence of kerogen contents and other factors in a quantitative and accurate way. We can build several kerogen models with the same background elastic moduli but different kerogen contents. As shown in Figure 11, the total volume of pores and kerogens in the digital core is 9.43%. We gradually filled some pores with kerogens to increase the kerogen content from 0% to 9.43%, producing a group of samples with
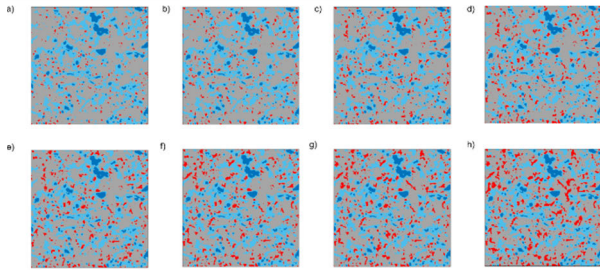
FIGURE 11. Digital core slices with kerogen contents of 1.99% (a), 2.99% (b), 4% (c), 4.98% (d), 6% (e), 6.95% (f), 7.91% (g), and 9.43% (h).
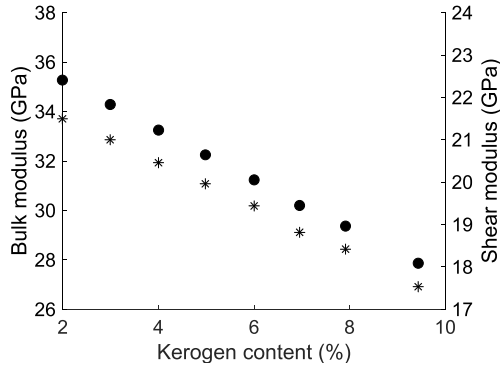

FIGURE 12. Effective bulk (dots) and shear (asterisks) moduli of each slice in Figures 11a-11h.

FIGURE 13. Digital core slices with different kerogen shapes generated by different rounding coefficients of 0.5 (a), 0.6 (b), 0.7 (c), 0.8 (d), 0.9 (e), and 1.0 (f).

FIGURE 14. Effective bulk (dots) and shear (asterisks) moduli of each slice in Figures 13a-13f.

FIGURE 15. A digital core slice 390 μm $\times$ 390 μm in size that contains 600 $\times$ 600 pixels. The slice represents porous media, but each pixel is actually a single-phase medium.

different kerogen contents. Figures 11a-11h show digital core slices with kerogen contents of 1.99%, 2.99%, 4%, 4.98%, 6%, 6.95%, 7.91%, and 9.43%, respectively. The red spots denote kerogens, light blue denotes mineral type 2, gray denotes mineral type 3, and dark blue denotes pyrite.

The effect of kerogen contents on porosity can be ignored [61], [62] because the correlation between porosity and kerogens in shales is not obvious. The bulk and shear moduli of mature kerogens that are used in this study are $K_k = 5.0\,\text{GPa}$ and $G_k = 3.5\,\text{GPa}$, respectively [1]. FE numerical modeling is conducted for the effective elastic moduli of each slice in Figures 11a-11h, with the results shown in Figure 12. The effective bulk (dots) and shear (asterisks) moduli decrease with increasing kerogen contents because of the much smaller moduli of kerogens than minerals. Therefore, the increase in kerogen content causes a decrease in the effective elastic moduli of organic shales.

D. EFFECT OF KEROGEN MORPHOLOGIES ON EFFECTIVE ELASTIC PROPERTIES

The elastic properties of organic shales may also be affected by kerogen shapes. Figure 13 shows several kerogen models with the same background elastic moduli and kerogen content (7.4%) but different kerogen morphologies that are generated by random media with different values of the rounding coefficient n. The rounding coefficient gradually increases from 0.5 to 1.0, as shown in Figures 13a-13f. Similarly, the red spots denote kerogens, light blue denotes mineral type 2, gray denotes mineral type 3, and dark blue denotes pyrite.
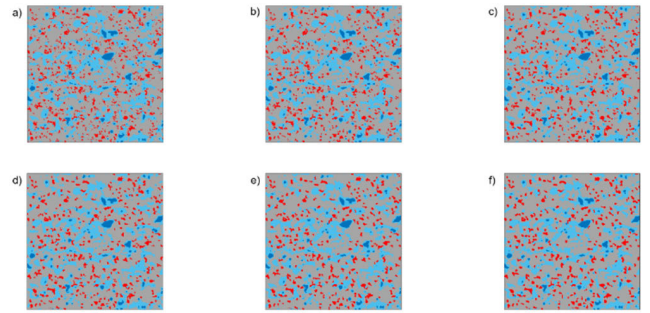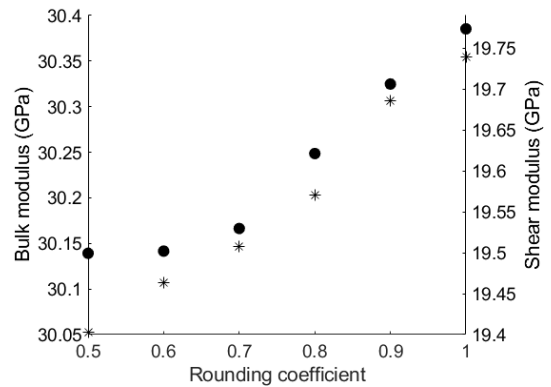
FE numerical modeling is conducted for the effective elastic moduli of each slice, with the results shown in Figure 14. With increasing coefficients, kerogen particles tend to be smooth at the edge, and the corresponding bulk (dots) and shear (asterisks) moduli increase. In general, rough kerogen particles are easier to compress than round particles and have smaller elastic moduli. Compared with Figure 12, the effect of kerogen shapes is much less than that of kerogen contents.

IV. ULTRASONIC SIMULATION OF ORGANIC MATTER

The ultrasonic response of organic matter provides insight into the geophysical prediction of sweet spots. It is also
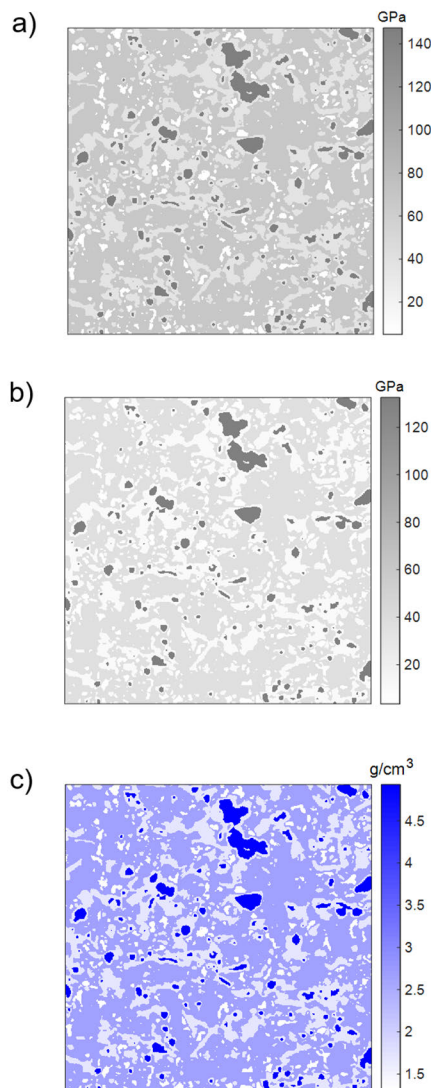
FIGURE 16. The resulting effective bulk (a), shear moduli (b) and density (c) for the digital core slice shown in Figure 15.

essential to interpret the heterogeneity of organic shales in terms of their scattering characteristics. Laboratory ultrasonic measurements illustrate that wave propagation in organic shales is an extremely complex process. The interaction between waves and microstructures as small-scale random heterogeneities involves strong scattering. Numerical simulation of ultrasonic responses in organic shales provides a supplementary means to interpret sonic measurements.

Numerical simulation of elastic wave propagation in shales faces several major challenges. First, unlike sandstones, shales are characterized by compliant microstructures (e.g., lenticular kerogens, bedding laminae, clay aggregates, and microcracks), which are difficult to capture but significantly affect wave propagation. We need higher-frequency waves to detect such heterogeneities, which challenge the accuracy and stability of numerical algorithms. Second, digital cores only provide an image of the gray distribution of microstructures (pores and minerals). Numerical simulation needs a
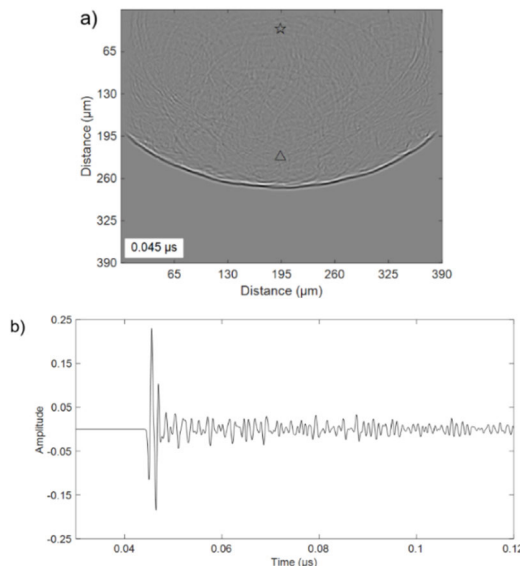
FIGURE 17. Snapshot (a) and waveform at receiver (b) for the digital core slice shown in Figure 15.

reasonable digital porous model with poroelastic properties reflecting the characteristics of true rocks. Megahertz ultrasound causes strong boundary reflections on the side ends of a core, which seriously interfere with ultrasonic coda and affect the accuracy of scattering analyses. In this section, we apply the RSG-FD numerical simulation of Biot's poroelastic equations (see Appendix B) to ultrasonic wave propagation in digital organic shales, followed by a coda analysis of ultrasonic scatterings with kerogen contents and morphologies.

A. DOUBLE-PHASE MEDIUM MODEL

Figure 15 shows a digital core slice $390 \, \mu m \times 390 \, \mu m$ in size that contains 600×600 pixels. The red spots denote kerogens, light blue denotes mineral type 2, gray denotes mineral type 3, and dark blue denotes pyrite. The slice represents porous media, but each pixel is actually a single-phase medium, either a solid (quartz grains) or a pores (interstitial clays/fluids). To make Biot's poroelastic equations applicable for numerical simulation, we need to build a digital core model as a double-phase medium. Based on the concept of a real reservoir of oil/gas, the fluid always exists as a mixture with quartz/clays rather than a pure fluid pool. Therefore, in this study, the fluid (oil) is assumed to be uniformly distributed in the whole background of a digital core to make the model a heterogeneous double-phase medium. That is, each pixel, as a mixture of oil with either quartz grains or interstitial clays residing in pores, is a double-phase medium and has both solid and liquid parameters.

We need to define reasonable physical properties for each pixel. According to the proportion of minerals inside a pixel, the average moduli can be calculated by FE modeling using the basic rock physical parameters, such as bulk moduli, shear moduli, and densities listed in Table 2. The resulting effective elastic moduli and density are shown in Figure 16. In the numerical simulation, the grid interval $\Delta x = \Delta z = 0.65 \, \mu m$,
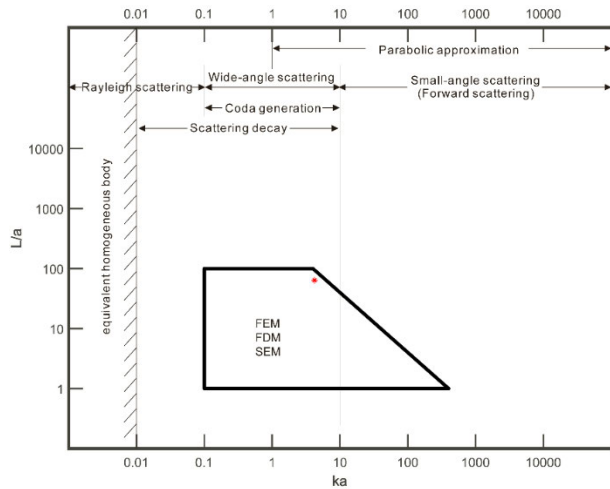
FIGURE 18. *L/a-ka* scatter mode and the distribution of digital core scatter intensity.
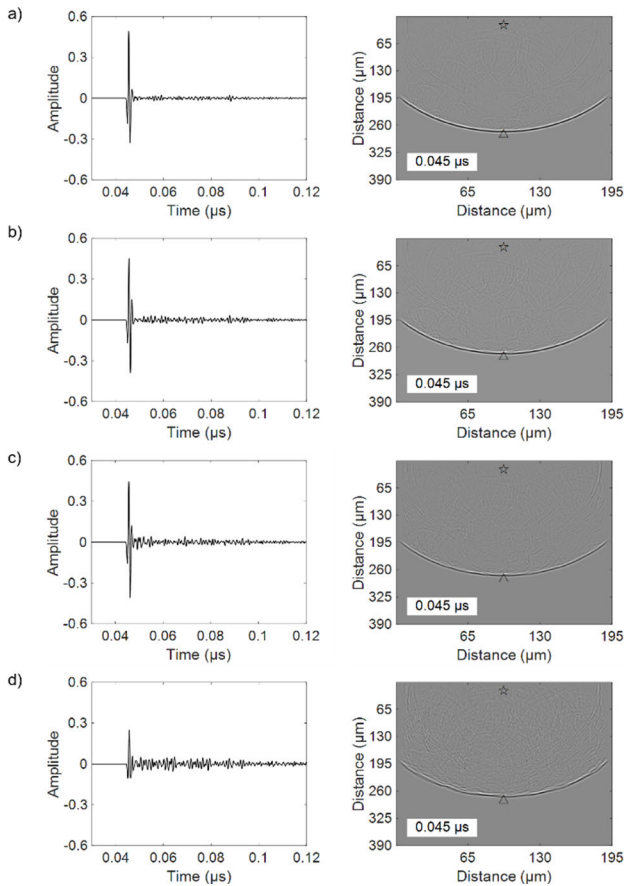

FIGURE 19. The waveforms at the receiver indicated by the triangle (left) and wavefield snapshots at 0.045 μs (right) for kerogen contents of 1.99% (a), 2.99% (b), 4% (c), and 7.91% (d).

FIGURE 20. The waveforms at the receiver indicated by the triangle (left) and wavefield snapshots at 0.045 μs (right) for rounding coefficients of 0.5 (a), 0.6 (b), 0.7 (c), and 1.0 (d).

FIGURE 21. Kerogen content (a) and rounding coefficient (b) versus Q^{-1}.

time interval $\Delta t = 0.00000015$ ms, time length T = 8000Δt, and P-wave velocity V = 4506 m/s. The excitation source (indicated by an asterisk), as shown in Figure 17a, is located at x = 300Δx and z = 30Δz in the slice. The receiver (indicated by a triangle) is located at x = 300Δx and z = 430Δz. There is a clear onset of maximum amplitude as direct waves occur in

the snapshot (Figure 17a) and waveforms occur at the receiver (Figure 17b). Wave scattering as a superposition of incoherent high-frequency scattered waves exhibits strong attenuation due to small-scale random heterogeneities. Figure 17 demonstrates the formation of coda as continuous waves in the tail portion of wave trains.

The digital core heterogeneity characteristics and scattering intensity can be represented by the *L/a-ka* distribution diagram (Figure 18), where the average rock heterogeneity characteristic length a is 3.88 μm, the ultrasonic wavenumber k is 1.12×10^6 m^{-1}, and the wave propagation distance L is 2.6×10^{-4} m. It is assumed that the excitation ultrasonic frequency is 800 MHz. Figure 18 reflects the correlation

between the medium inhomogeneous scale and the wavelength scale.

B. EFFECT OF KEROGEN CONTENTS ON ULTRASONIC RESPONSES

The RSG-FD numerical method of Biot's poroelastic equations described in Appendix B is conducted to simulate ultrasonic wave propagation in the digital core slices, as shown in Figures 11a-11h. Figure 19 shows the waveforms at the receiver indicated by the triangle (left) and wavefield snapshots at 0.045 μs (right) for kerogen contents of 1.99% (a), 2.99% (b), 4% (c), and 7.91% (d). The scattering effect becomes stronger with increasing kerogen content, which reduces the energy of coherent wavefields. The attenuation is stronger at high kerogen contents, as shown in Figure 21a, since the elastic modulus of kerogen is much smaller than that of the mineral.

C. EFFECT OF KEROGEN MORPHOLOGIES ON ULTRASONIC RESPONSES
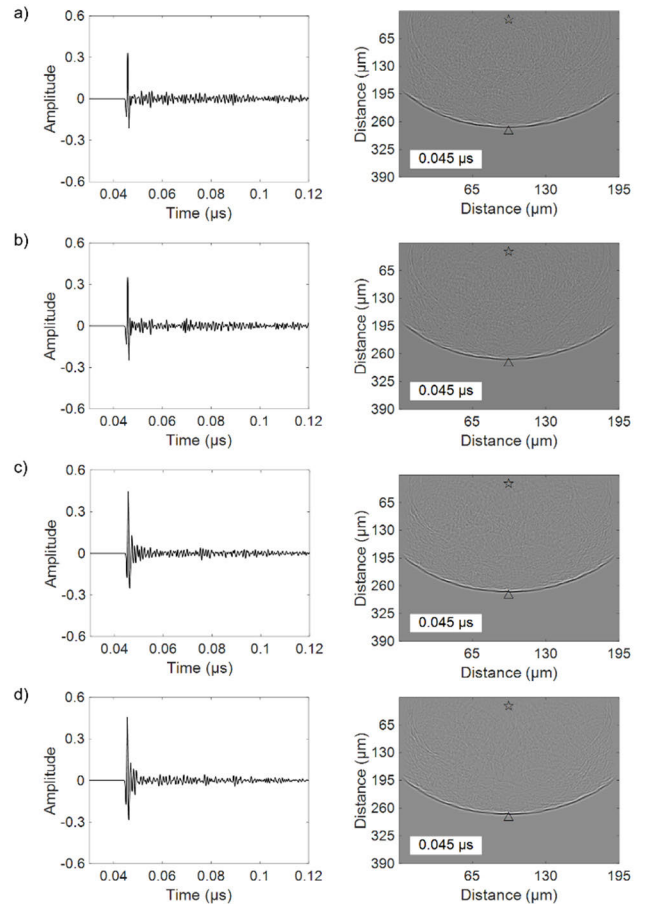
In terms of the effects of the kerogen morphologies, Figure 20 shows the waveforms at the receiver indicated by the triangle (left) and wavefield snapshots at 0.045 μs (right) for rounding coefficients of 0.5 (a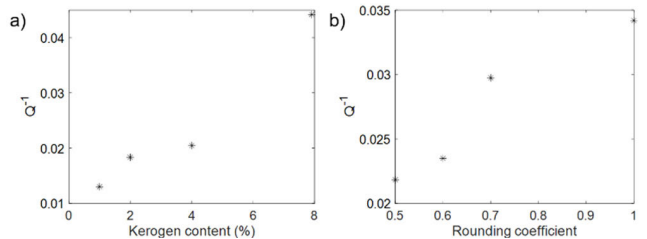), 0.6 (b), 0.7 (c), and 1.0 (d). The scattering effect becomes weaker with increasing rounding coefficients. The attenuation is stronger when rounding coefficients are smaller, as shown in Figure 21b, because when the rounding coefficient is small, the particle edges are rough and the particles are relatively dispersed, the kerogen is difficult to compress due to the effects related to the Poisson ratio.

V. CONCLUSION

Organic shales usually exhibit significant heterogeneity as a result of multiscale components, which also affect their elastic properties and acoustic response. We propose a multiscale random media method to reconstruct kerogen distributions for a group of digital shale cores with different kerogen contents and morphologies and model their effective elastic properties, followed by a simulation of acoustic responses. The main conclusions are as follows:

1) The reconstruction of the spatial distribution of organic matter plays an important role in determining development schemes. The size, density, and morphology of organic matter are distributed heterogeneously, even inside the same sedimentary facies, which makes the conventional single-scale method difficult to apply. The multiscale method can not only describe the microscopic heterogeneity of kerogens more precisely but also provide the feasibility to study the seismic response of individual shale components. Therefore, multiscale media reconstruction is an effective method to reconstruct the distribution and morphology of heterogeneous kerogens.

2) We validate that the finite-element method is universally valid for general elastic modulus modeling of complex organic shales. Kerogen contents and morphologies significantly influence the effective elasticity of organic shales. Numerical investigations of effective elastic properties conducted for shale samples with different contents and morphologies of organic matter show that the increase in kerogen content and the decrease in the rounding coefficient n, which determines the morphology parameter of kerogens, leads to a decrease in the elastic modulus of organic shale.

3) We conduct a numerical simulation of ultrasonic responses by applying the rotated staggered-grid finite difference method to Biot's poroelastic equations, followed by a coda analysis of ultrasonic scatterings. The ultrasonic responses are mainly affected by kerogen contents, with less influence by organic matter morphologies. The scattering effects become stronger for higher kerogen contents with smaller rounding coefficients.

APPENDIX A

The geometry of rock particles formed in different sedimentary environments varies greatly, and the conventional random medium model cannot adapt to this multiscale situation. Xi and Yao [21] propose an intermixed random media model, and the autocorrelation function is as follows:

$$\varphi(x, z) = exp\left[-\left(\frac{x^2}{a^2} + \frac{z^2}{b^2}\right)^n\right], \quad \text{(A-1)}$$

where a and b are the autocorrelation lengths in the x and z directions, respectively, and n is the rounding coefficient. If the values of a and b are fixed, the value of n determines the attenuation degree of φ with the change of x and z. The larger n is, the smoother the boundary of the reconstructed rock particle is. Conversely, the smaller n is, the more irregular the boundary of the reconstructed rock particle is. The average particle size can be controlled by fixing the n value and changing a and b. In particular, the intermixed model degenerates into exponential type and Gaussian type when $n = 0.5$ and 1, respectively. Therefore, a and b reflect the average scale of particles in the horizontal and vertical directions, and the rounding coefficient n controls the roughness of particle edges.

The direction factor $\theta \in [0, 2\pi)$ is introduced into the intermixed random media model to obtain a vector intermixed random media model [63], whose autocorrelation function is as follows:

$$\varphi(x, z)$$
$$= exp\left\{-\left[\frac{(x\cos\theta + z\sin\theta)^2}{a^2} + \frac{(x\sin\theta - z\cos\theta)^2}{b^2}\right]^n\right\}. \quad \text{(A-2)}$$

The vector model degenerates into an intermixed model when $\theta = 0$.

APPENDIX B

Biot's equation for isotropic porous media saturated with a viscous fluid is as follows [64], [65]:

$$
\begin{cases}
\rho_b \ddot{u}_i + \rho_f \ddot{w}_i = (\lambda + \mu + \alpha^2 M)\, u_{j,ji} + \mu u_{i,jj} + \alpha M w_{j,ji} \\
\rho_f \ddot{u}_i + \rho_m \ddot{w}_i + b\dot{w}_i = M(\alpha u_{j,ji} + w_{j,ji}),
\end{cases}
$$
(B-1)

where u_i is the displacement component of the solid phase, U_i is the displacement component of the fluid phase, λ and μ are the Lamé constants of the drained matrix, and the quantity $\rho_b = (1 - \phi)\,\rho_s + \phi\rho_f$ is the composite density, with ρ_s and ρ_f being the solid and fluid densities, respectively. ϕ is the porosity. Darcy's law defines the movement of viscous fluids of viscosity η in the frame of permeability χ, and $b = \eta/\chi$. $\rho_m = \tau\rho_f/\phi$, with τ being the tortuosity:

$$
\begin{cases}
\alpha = 1 - \dfrac{K_m}{K_s}, \quad K_m = \lambda + \dfrac{2}{3}\mu \\[2mm]
M = \dfrac{K_s}{1 - \phi - \dfrac{K_m}{K_s} + \phi\dfrac{K_s}{K_f}} \\[4mm]
w_i = \phi\,(U_i - u_i),
\end{cases}
$$
(B-2)

where K_s and K_f are the solid and fluid bulk moduli, respectively.

The discrete format of each physical quantity in the L-order rotated staggered-grid FD is as follows [66]:

$$
\begin{aligned}
\frac{\partial v_i}{\partial x}\Big|_{(x,z)}
&= \sum_{n=1}^{L/2} \frac{c_n}{2\Delta x}\Big\{ v_i\big|_{\left(x+\left(n-\frac{1}{2}\right),z+\left(n-\frac{1}{2}\right)\right)} \\
&\quad + v_i\big|_{\left(x+\left(n-\frac{1}{2}\right),z-\left(n-\frac{1}{2}\right)\right)} - v_i\big|_{\left(x-\left(n-\frac{1}{2}\right),z-\left(n-\frac{1}{2}\right)\right)} \\
&\quad - v_i\big|_{\left(x-\left(n-\frac{1}{2}\right),z+\left(n-\frac{1}{2}\right)\right)} \Big\},
\end{aligned}
$$
(B-3)

$$
\begin{aligned}
\frac{\partial v_i}{\partial z}\Big|_{(x,z)}
&= \sum_{n=1}^{L/2} \frac{c_n}{2\Delta z}\Big\{ v_i\big|_{\left(x+\left(n-\frac{1}{2}\right),z+\left(n-\frac{1}{2}\right)\right)} \\
&\quad - v_i\big|_{\left(x+\left(n-\frac{1}{2}\right),z-\left(n-\frac{1}{2}\right)\right)} - v_i\big|_{\left(x-\left(n-\frac{1}{2}\right),z-\left(n-\frac{1}{2}\right)\right)} \\
&\quad + v_i\big|_{\left(x-\left(n-\frac{1}{2}\right),z+\left(n-\frac{1}{2}\right)\right)} \Big\},
\end{aligned}
$$
(B-4)

$$
\begin{aligned}
\frac{\partial q_i}{\partial x}\Big|_{(x,z)}
&= \sum_{n=1}^{L/2} \frac{c_n}{2\Delta x}\Big\{ q_i\big|_{\left(x+\left(n-\frac{1}{2}\right),z+\left(n-\frac{1}{2}\right)\right)} \\
&\quad + q_i\big|_{\left(x+\left(n-\frac{1}{2}\right),z-\left(n-\frac{1}{2}\right)\right)} - q_i\big|_{\left(x-\left(n-\frac{1}{2}\right),z-\left(n-\frac{1}{2}\right)\right)} \\
&\quad - q_i\big|_{\left(x-\left(n-\frac{1}{2}\right),z+\left(n-\frac{1}{2}\right)\right)} \Big\},
\end{aligned}
$$
(B-5)

$$
\frac{\partial q_i}{\partial z}\Big|_{(x,z)}
= \sum_{n=1}^{L/2} \frac{c_n}{2\Delta z}\Big\{ q_i\big|_{\left(x+\left(n-\frac{1}{2}\right),z+\left(n-\frac{1}{2}\right)\right)}
$$

$$
\begin{aligned}
&\quad - q_i\big|_{\left(x+\left(n-\frac{1}{2}\right),z-\left(n-\frac{1}{2}\right)\right)} - q_i\big|_{\left(x-\left(n-\frac{1}{2}\right),z-\left(n-\frac{1}{2}\right)\right)} \\
&\quad + q_i\big|_{\left(x-\left(n-\frac{1}{2}\right),z+\left(n-\frac{1}{2}\right)\right)} \Big\},
\end{aligned}
$$
(B-6)

$$
\begin{aligned}
\frac{\partial \tau_{ij}}{\partial x}\Big|_{\left(x+\frac{1}{2},z+\frac{1}{2}\right)}
&= \sum_{n=1}^{L/2} \frac{c_n}{2\Delta x}\Big\{ \tau_{ij}\big|_{(x+n,z+n)} + \tau_{ij}\big|_{(x+n,z-(n-1))} \\
&\quad - \tau_{ij}\big|_{(x-n,z-(n-1))} - \tau_{ij}\big|_{(x-n,z+n)} \Big\},
\end{aligned}
$$
(B-7)

$$
\begin{aligned}
\frac{\partial \tau_{ij}}{\partial z}\Big|_{\left(x+\frac{1}{2},z+\frac{1}{2}\right)}
&= \sum_{n=1}^{L/2} \frac{c_n}{2\Delta z}\Big\{ \tau_{ij}\big|_{(x+n,z+n)} - \tau_{ij}\big|_{(x+n,z-(n-1))} \\
&\quad - \tau_{ij}\big|_{(x-n,z-(n-1))} + \tau_{ij}\big|_{(x-n,z+n)} \Big\},
\end{aligned}
$$
(B-8)

$$
\begin{aligned}
\frac{\partial p}{\partial x}\Big|_{\left(x+\frac{1}{2},z+\frac{1}{2}\right)}
&= \sum_{n=1}^{L/2} \frac{c_n}{2\Delta x}\Big\{ p\big|_{(x+n,z+n)} + p\big|_{(x+n,z-(n-1))} \\
&\quad - p\big|_{(x-n,z-(n-1))} - p\big|_{(x-n,z+n)} \Big\},
\end{aligned}
$$
(B-9)

$$
\begin{aligned}
\frac{\partial p}{\partial z}\Big|_{\left(x+\frac{1}{2},z+\frac{1}{2}\right)}
&= \sum_{n=1}^{L/2} \frac{c_n}{2\Delta z}\Big\{ p\big|_{(x+n,z+n)} - p\big|_{(x+n,z-(n-1))} \\
&\quad - p\big|_{(x-n,z-(n-1))} + p\big|_{(x-n,z+n)} \Big\},
\end{aligned}
$$
(B-10)

where c_n is the difference coefficient.

The CPML formulas of the poroelastic equations are as follows [66]:

$$
\begin{aligned}
\rho\dot{v}_x &= \rho_m\left(\frac{1}{\chi_x}\partial_x\tau_{xx} + \psi_{x,\tau_{xx}} + \frac{1}{\chi_z}\partial_z\tau_{xz} + \psi_{z,\tau_{xz}} \right) \\
&\quad + \rho_f\left(\frac{1}{\chi_x}\partial_x p + \psi_{x,p} \right) + \rho_f b q_x,
\end{aligned}
$$
(B-11)

$$
\begin{aligned}
\rho\dot{v}_z &= \rho_m\left(\frac{1}{\chi_x}\partial_x\tau_{xz} + \psi_{x,\tau_{xz}} + \frac{1}{\chi_z}\partial_z\tau_{zz} + \psi_{z,\tau_{zz}} \right) \\
&\quad + \rho_f\left(\frac{1}{\chi_z}\partial_z p + \psi_{z,p} \right) + \rho_f b q_z,
\end{aligned}
$$
(B-12)

$$
\begin{aligned}
\rho\dot{q}_x &= -\rho_f\left(\frac{1}{\chi_x}\partial_x\tau_{xx} + \psi_{x,\tau_{xx}} + \frac{1}{\chi_z}\partial_z\tau_{xz} + \psi_{z,\tau_{xz}} \right) \\
&\quad - \rho_b\left(\frac{1}{\chi_x}\partial_x p + \psi_{x,p} \right) - \rho_b b q_x,
\end{aligned}
$$
(B-13)

$$
\begin{aligned}
\rho\dot{q}_z &= -\rho_f\left(\frac{1}{\chi_x}\partial_x\tau_{xz} + \psi_{x,\tau_{xz}} + \frac{1}{\chi_z}\partial_z\tau_{zz} + \psi_{z,\tau_{zz}} \right) \\
&\quad - \rho_b\left(\frac{1}{\chi_z}\partial_z p + \psi_{z,p} \right) - \rho_b b q_z,
\end{aligned}
$$
(B-14)

$$
\begin{aligned}
\dot{\tau}_{xx} &= (\lambda_u + 2\mu)\left(\frac{1}{\chi_x}\partial_x v_x + \psi_{x,v_x} \right) \\
&\quad + \beta M\left(\frac{1}{\chi_x}\partial_x q_x + \psi_{x,q_x} \right),
\end{aligned}
$$
(B-15)

$$
\begin{aligned}
\dot{\tau}_{zz} &= (\lambda_u + 2\mu)\left(\frac{1}{\chi_z}\partial_z v_z + \psi_{z,v_z} \right) \\
&\quad + \beta M\left(\frac{1}{\chi_z}\partial_z q_z + \psi_{z,q_z} \right),
\end{aligned}
$$
(B-16)

$$\dot{\tau}_{xz} = \mu \left(\frac{1}{\chi_z} \partial_z v_x + \psi_{z,v_x} + \frac{1}{\chi_x} \partial_x v_z + \psi_{x,v_z} \right), \quad \text{(B-17)}$$

$$\dot{p} = -\beta M \left(\frac{1}{\chi_x} \partial_x v_x + \psi_{x,v_x} + \frac{1}{\chi_z} \partial_z v_z + \psi_{z,v_z} \right)$$
$$- M \left(\frac{1}{\chi_x} \partial_x q_x + \psi_{x,q_x} + \frac{1}{\chi_z} \partial_z q_z + \psi_{z,q_z} \right). \quad \text{(B-18)}$$

REFERENCES

[1] L. Zhao, X. Qin, D.-H. Han, J. Geng, Z. Yang, and H. Cao, "Rock-physics modeling for the elastic properties of organic shale at different maturity stages," *Geophysics*, vol. 81, no. 5, pp. D527–D541, Sep. 2016.

[2] H. Andrä, N. Combaret, J. Dvorkin, E. Glatt, J. Han, M. Kabel, Y. Keehm, F. Krzikalla, M. Lee, C. Madonna, M. Marsh, T. Mukerji, E. H. Saenger, R. Sain, N. Saxena, S. Ricker, A. Wiegmann, and X. Zhan, "Digital rock physics benchmarks—Part II: Computing effective properties," *Comput. Geosci.*, vol. 50, pp. 33–43, Jan. 2013.

[3] J. Dvorkin, N. Derzhi, E. Diaz, and Q. Fang, "Relevance of computational rock physics," *Geophysics*, vol. 76, no. 5, pp. E141–E153, Sep. 2011.

[4] M. Josh, L. Esteban, C. Delle Piane, J. Sarout, D. N. Dewhurst, and M. B. Clennell, "Laboratory characterisation of shale properties," *J. Petroleum Sci. Eng.*, vols. 88–89, pp. 107–124, Jun. 2012.

[5] L. Vernik and C. Landis, "Elastic anisotropy of source rocks: Implications for hydrocarbon generation and primary migration1," *AAPG Bull.*, vol. 80, no. 4, pp. 531–544, Apr. 1996.

[6] T. Vanorio, T. Mukerji, and G. Mavko, "Emerging methodologies to characterize the rock physics properties of organic-rich shales," *Lead. Edge*, vol. 27, no. 6, pp. 780–787, Jun. 2008.

[7] S. Zargari, M. Prasad, K. C. Mba, and E. D. Mattson, "Organic maturity, elastic properties, and textural characteristics of self resourcing reservoirs," *Geophysics*, vol. 78, no. 4, pp. D223–D235, Jul. 2013.

[8] M. R. Yenugu, "Elastic, microstructural and geochemical characterization of kerogen maturity for shales," Ph.D. dissertation, Univ. Houston, Houston, TX, USA, May 2014.

[9] C. M. Sayers, "The effect of kerogen on the elastic anisotropy of organic-rich shales," *Geophysics*, vol. 78, no. 2, pp. D65–D74, Mar. 2013.

[10] M. S. Talukdar, O. Torsaeter, M. A. Ioannidis, and J. J. Howard, "Stochastic reconstruction, 3D characterization and network modeling of chalk," *J. Petroleum Sci. Eng.*, vol. 35, nos. 1–2, pp. 1–21, Jul. 2002.

[11] B. Biswal, P.-E. Øren, R. J. Held, S. Bakke, and R. Hilfer, "Stochastic multiscale model for carbonate rocks," *Phys. Rev. E, Stat. Phys. Plasmas Fluids Relat. Interdiscip. Top.*, vol. 75, no. 6, Jun. 2007, Art. no. 061303.

[12] P. Tahmasebi, A. Hezarkhani, and M. Sahimi, "Multiple-point geostatistical modeling based on the cross-correlation functions," *Comput. Geosci.*, vol. 16, no. 3, pp. 779–797, Jun. 2012.

[13] K. M. Gerke, M. V. Karsanina, and D. Mallants, "Universal stochastic multiscale image fusion: An example application for shale rock," *Sci. Rep.*, vol. 5, no. 1, p. 15880, Nov. 2015.

[14] Y. Wu, C. Lin, L. Ren, W. Yan, S. An, B. Chen, Y. Wang, X. Zhang, C. You, and Y. Zhang, "Reconstruction of 3D porous media using multiple-point statistics based on a 3D training image," *J. Natural Gas Sci. Eng.*, vol. 51, pp. 129–140, Mar. 2018.

[15] L. Ji, M. Lin, G. Cao, and W. Jiang, "A core-scale reconstructing method for shale," *Sci. Rep.*, vol. 9, no. 1, pp. 1–12, Mar. 2019.

[16] A. Frankel and R. W. Clayton, "A finite-difference simulation of wave propagation in two-dimensional random media," *Bull. Seismolog. Soc. Amer.*, vol. 74, no. 6, pp. 2167–2186, Dec. 1984.

[17] M. Roth and M. Korn, "Single scattering theory versus numerical modelling in 2-D random media," *Geophys. J. Int.*, vol. 112, no. 1, pp. 124–140, Jan. 1993.

[18] L. T. Ikelle, S. K. Yung, and F. Daube, "2-D random media with ellipsoidal autocorrelation functions," *Geophysics*, vol. 58, no. 9, pp. 1359–1372, Sep. 1993.

[19] S. Painter and L. Paterson, "Fractional Lévy motion as a model for spatial variability in sedimentary rock," *Geophys. Res. Lett.*, vol. 21, no. 25, pp. 2857–2860, Dec. 1994.

[20] T. M. Müller and S. A. Shapiro, "Green's function construction for 2D and 3D elastic random media," in *SEG Tech. Program Expanded Abstr.*, vol. 18, no. 1, pp. 1797–1800, Jan. 1999.

[21] X. Xi and Y. Yao, "Simulations of random medium model and intermixed random medium," (in Chinese), *Earth Sci.-J. China Univ. Geosci.*, vol. 27, no. 1, pp. 67–71, Jan. 2002.

[22] C. D. Boateng and L.-Y. Fu, "Analysis of reservoir heterogeneities and depositional environments: A new method," *Explor. Geophys.*, vol. 49, no. 6, pp. 868–880, Nov. 2018.

[23] B. E. Hornby, L. M. Schwartz, and J. A. Hudson, "Anisotropic effective-medium modeling of the elastic properties of shales," *Geophysics*, vol. 59, no. 10, pp. 1570–1583, Oct. 1994.

[24] A. M. Lucier, R. Hofmann, and L. T. Bryndzia, "Evaluation of variable gas saturation on acoustic log data from the haynesville shale gas play, NW Louisiana, USA," *Lead. Edge*, vol. 30, no. 3, pp. 300–311, Mar. 2011.

[25] J. M. Carcione, H. B. Helle, and P. Avseth, "Source-rock seismic-velocity models: Gassmann versus backus," *Geophysics*, vol. 76, no. 5, pp. N37–N45, Sep. 2011.

[26] J. M. Carcione and P. Avseth, "Rock-physics templates for clay-rich source rocks," *Geophysics*, vol. 80, no. 5, pp. D481–D500, Sep. 2015.

[27] Y. Zhu, S. Xu, M. Payne, A. Martinez, E. Liu, C. Harris, and K. Bandyopadhyay, "Improved rock-physics model for shale gas reservoirs," in *SEG Technical Program Expanded Abstracts*. Tulsa, OK, USA: Society of Exploration Geophysicists, Sep. 2012, pp. 1–5.

[28] B. Y. Fu, L. Y. Fu, C. H. Cao, and T. C. Han, "The analysis of the influence of organic content on the elastic properties of shale based on solid substitution model," (in Chinese), *Chin. J. Geophys.*, vol. 63, no. 7, pp. 2823–2835, Jul. 2020.

[29] X. Han, J. Nie, J. Guo, L. Yang, and D. Xu, "Rock physics modelling of elastic properties of organic shale considering kerogen stress and pore pressure distribution," *J. Petroleum Sci. Eng.*, vol. 174, pp. 891–902, Mar. 2019.

[30] E. J. Garboczi and A. R. Day, "An algorithm for computing the effective linear elastic properties of heterogeneous materials: Three-dimensional results for composites with equal phase Poisson ratios," *J. Mech. Phys. Solids*, vol. 43, no. 9, pp. 1349–1362, Sep. 1995.

[31] A. P. Roberts and E. J. Garboczi, "Elastic properties of model porous ceramics," *J. Amer. Ceram. Soc.*, vol. 83, no. 12, pp. 3041–3048, Dec. 2000.

[32] C. H. Arns, M. A. Knackstedt, W. V. Pinczewski, and E. J. Garboczi, "Computation of linear elastic properties from microtomographic images: Methodology and agreement between theory and experiment," *Geophysics*, vol. 67, no. 5, pp. 1396–1405, Sep. 2002.

[33] J. Dvorkin, Q. Fang, and N. Derzhi, "Etudes in computational rock physics: Alterations and benchmarking," *Geophysics*, vol. 77, no. 3, pp. D45–D52, May 2012.

[34] Y. Zhang, L.-Y. Fu, L. Zhang, W. Wei, and X. Guan, "Finite difference modeling of ultrasonic propagation (coda waves) in digital porous cores with un-split convolutional PML and rotated staggered grid," *J. Appl. Geophys.*, vol. 104, pp. 75–89, May 2014.

[35] W. Ru-Shan, "Attenuation of short period seismic waves due to scattering," *Geophys. Res. Lett.*, vol. 9, no. 1, pp. 9–12, Jan. 1982.

[36] O. Nishizawa, T. Satoh, X. Lei, and Y. Kuwahara, "Laboratory studies of seismic wave propagation in inhomogeneous media using a laser Doppler vibrometer," *Bull. Seismological Soc. Amer.*, vol. 87, no. 4, pp. 809–823, Aug. 1997.

[37] H. Sato and M. Fehler, *Seismic Wave Propagation and Scattering in the Heterogeneous Earth*. Berlin, Germany: Springer-Verlag, 1998.

[38] M. Fehler, "Interaction of seismic waves with a viscous liquid layer," *Bull. Seismological Soc. Amer.*, vol. 72, no. 1, pp. 55–72, 1982.

[39] K. Aki, "Analysis of the seismic coda of local earthquakes as scattered waves," *J. Geophys. Res.*, vol. 74, no. 2, pp. 615–631, Jan. 1969.

[40] K. Aki and B. Chouet, "Origin of coda waves: Source, attenuation, and scattering effects," *J. Geophys. Res.*, vol. 80, no. 23, pp. 3322–3342, Aug. 1975.

[41] J. M. Carcione and G. Quiroga-Goode, "Some aspects of the physics and numerical modeling of Biot compressional waves," *J. Comput. Acoust.*, vol. 3, no. 4, pp. 261–280, Dec. 1995.

[42] J. M. Carcione and H. B. Helle, "Numerical solution of the poroviscoelastic wave equation on a staggered mesh," *J. Comput. Phys.*, vol. 154, no. 2, pp. 520–527, Sep. 1999.

[43] A. Grêt, R. Snieder, and J. Scales, "Time-lapse monitoring of rock properties with coda wave interferometry," *J. Geophys. Res. Solid Earth*, vol. 111, no. B3, pp. B03305-1–B03305-11, Mar. 2006.

[44] Y. J. Masson and S. R. Pride, "Poroelastic finite difference modeling of seismic attenuation and dispersion due to mesoscopic-scale heterogeneity," *J. Geophys. Res.*, vol. 112, no. B3, pp. B03204-1–B03204-16, Mar. 2007.

[45] F. Wenzlau and T. M. Müller, "Finite-difference modeling of wave propagation and diffusion in poroelastic media," *Geophysics*, vol. 74, no. 4, pp. T55–T66, Jul. 2009.

[46] W. Wei and L.-Y. Fu, "Monte Carlo simulation of stress-associated scattering attenuation from laboratory ultrasonic measurements," *Bull. Seismological Soc. Amer.*, vol. 104, no. 2, pp. 931–943, Apr. 2014.

[47] E. H. Saenger, N. Gold, and S. A. Shapiro, "Modeling the propagation of elastic waves using a modified finite-difference grid," *Wave Motion*, vol. 31, no. 1, pp. 77–92, Jan. 2000.

[48] E. H. Saenger and S. A. Shapiro, "Effective velocities in fractured media: A numerical study using the rotated staggered finite-difference grid," *Geophys. Prospecting*, vol. 50, no. 2, pp. 183–194, Nov. 2002.

[49] D. Komatitsch and R. Martin, "An unsplit convolutional perfectly matched layer improved at grazing incidence for the seismic wave equation," *Geophysics*, vol. 72, no. 5, pp. SM155–SM167, Sep. 2007.

[50] R. Martin and D. Komatitsch, "An unsplit convolutional perfectly matched layer technique improved at grazing incidence for the viscoelastic wave equation," *Geophys. J. Int.*, vol. 179, no. 1, pp. 333–344, Oct. 2009.

[51] V. Hucka and B. Das, "Brittleness determination of rocks by different methods," *Sci. Geomech. Abstr.*, vol. 11, no. 10, pp. 389–392, 1974.

[52] D. M. Jarvie, R. J. Hill, T. E. Ruble, and R. M. Pollastro, "Unconventional shale-gas systems: The mississippian barnett shale of north-central texas as one model for thermogenic shale-gas assessment," *AAPG Bull.*, vol. 91, no. 4, pp. 475–499, Apr. 2007.

[53] X. J. Shen, X. Liu, and H. P. Chen, "Fast computation of threshold based on multi-threshold Otsu criterion," *J. Electron. Inf. Technol.*, vol. 39, no. 1, pp. 144–149, Jan. 2017.

[54] K. Pearson, "Notes on regression and inheritance in the case of two parents," *Proc. Roy. Soc. London*, vol. 58, pp. 240–242, Jan. 1895.

[55] W. Voigt, *Lehrbuch der Kristallphysik (mit Ausschluss der Kristalloptik)*. MI, USA: BG Teubner, 1910.

[56] G. Mavko, T. Mukerji, and J. Dvorkin, *The Rock Physics Handbook: Tools for Seismic Analysis in Porous Media*. Cambridge, U.K.: Cambridge Univ. Press, 1998.

[57] G. Simmons and F. Birch, "Elastic constants of pyrite," *J. Appl. Phys.*, vol. 34, no. 9, pp. 2736–2738, Sep. 1963.

[58] J. P. D. Blangy, "Integrated seismic lithologic interpretation: The petrophysical basis," Ph.D. dissertation, Dept. Geophys., School Earth Sci., Stanford Univ., Stanford, CA, USA, 1992.

[59] R. Ciz and S. A. Shapiro, "Generalization of gassmann equations for porous media saturated with a solid material," *Geophysics*, vol. 72, no. 6, pp. A75–A79, Nov. 2007.

[60] N. Saxena and G. Mavko, "Exact equations for fluid and solid substitution," *Geophysics*, vol. 79, no. 3, pp. L21–L32, May 2014.

[61] L. Vernik and A. Nur, "Ultrasonic velocity and anisotropy of hydrocarbon source rocks," *Geophysics*, vol. 57, no. 5, pp. 727–735, May 1992.

[62] L. Vernik and X. Liu, "Velocity anisotropy in shales: A petrophysical study," *Geophysics*, vol. 62, no. 2, pp. 521–532, Mar. 1997.

[63] L. W. Ma, Q. Y. Yang, H. M. Gu, J. Liu, Z. L. Lin, and S. S. Lyu, "Simulation of reservoir seismic response in the northern slope of the middle tarim basin with random fracture-cavern media model," (in Chinese), *Oil Geophys. Prospecting*, vol. 51, no. 6, pp. 1119–1127, Dec. 2016.

[64] M. A. Biot, "The theory of propagation of elastic waves in a fluid-saturated porous solid, I. Low-frequency range II. Higher frequency range," *J. Acoust. Soc. Amer.*, vol. 28, no. 2, pp. 168–191, Mar. 1956.

[65] M. A. Biot, "Mechanics of deformation and acoustic propagation in porous media," *J. Appl. Phys.*, vol. 33, no. 4, pp. 1482–1498, Apr. 1962.

[66] L. X. Zhang, L. Y. Fu, and Z. L. Pei, "Finite difference modeling of Biot's poroelastic equations with unsplit convolutional PML and rotated staggered grid," (in Chinese), *Chin. J. Geophys.*, vol. 53, no. 10, pp. 2470–2483, Oct. 2010.

YING RAO received the B.S. degree in geophysics from the China University of Petroleum, Beijing, China, in 2015. She is currently pursuing the Ph.D. degree with the Institute of Geology and Geophysics, Chinese Academy of Sciences. Her research interest includes rock physics.

LI-YUN FU received the B.S. degree in petroleum exploration from the Chengdu University of Technology, Chengdu, China, in 1985, and the M.S. and Ph.D. degrees in geophysics from the China University of Petroleum, Beijing, China, in 1992 and 1995, respectively.

From 1995 to 1997, he was a Postdoctoral Fellow in engineering mechanics with Tsinghua University. From 1997 to 1999, he was a Postdoctoral Fellow in tectonic structure with the University of California at Los Angeles (UCLA). From 1999 to 2004, he was a Research Scientist with the Commonwealth Scientific and Industrial Research Organization (CSIRO) and the Australian Resources Research Centre, and simultaneously, he was also a Visiting Professor with the College of Physics, Curtin University, Australia. From 2002 to 2003, he was a Visiting Researcher with the Institute of Geophysics and Planetary Physics (IGPP), UCLA. From 2004 to 2017, he was the Group Leader of Seismology at the Institute of Geology and Geophysics, Chinese Academy of Sciences, Beijing. Since 2017, he has been a Professor with the School of Geosciences, China University of Petroleum (East China), Qingdao, China. His research interests include regional seismic facies, crustal seismic wave propagation, seismic simulation, and imaging of complex geological structures.

ZHI-WEI WANG received the B.S. degree in geophysics from the China University of Geosciences, Wuhan, in 2014, and the Ph.D. degree in geophysics from the Institute of Geology and Geophysics, Chinese Academy of Sciences, in 2020. He is currently a Postdoctoral Fellow with the China University of Petroleum (East China). His research interests include rock physics and thermoelasticity problem.

BO-YE FU received the B.S. degree in geosciences from the China University of Geosciences, Beijing, in 2014, and the Ph.D. degree in geophysics from the Institute of Geology and Geophysics, Chinese Academy of Sciences (IGGCAS), in 2019. He is currently a Postdoctoral Fellow in geophysics with IGGCAS. His research interests include rock physics and acoustoelasticity.

● ● ●